

Observing localization and delocalization of the flat-band states in an acoustic cubic latticeYa-Xi Shen,^{1,2} Yu-Gui Peng,^{1,*} Pei-Chao Cao,¹ Jensen Li^{①,2} and Xue-Feng Zhu^{1,†}¹*School of Physics and Innovation Institute, Huazhong University of Science and Technology, Wuhan 430074, People's Republic of China*²*Department of Physics, The Hong Kong University of Science and Technology, Clear Water Bay, Hong Kong, China*

(Received 14 September 2021; revised 21 February 2022; accepted 23 February 2022; published 8 March 2022)

Over the past decades, wave localization and a wide variety of related phenomena have come to the forefront of research. Here, we theoretically and experimentally investigate the localization and delocalization of the flat-band states in an acoustic cubic lattice. Under evanescent couplings, the band structure of the designed cubic lattice has two dispersive bands and two degenerate flat bands. According to the analyses, we find that the constructions of flat-band states only depend on the excitation pressures and the coupling coefficients, which are frequency independent. With the flat-band state excitation, the acoustic wave can be either localized or delocalized in the lattice, which is determined by the excitation frequency. When the excitation frequency is close to the flat-band frequency of the lattice, the flat-band state can spread into the whole cubic lattice due to the resonance energy transfer among primitive cells. On the other hand, when the excitation frequency deviates from the flat-band frequency, the flat-band state can be localized in any primitive cell of the designed lattice. This work lays the groundwork for exploring the high-dimensional bound states in acoustic systems and has potential impacts on the applications of acoustic sensing and sound energy harvesting.

DOI: [10.1103/PhysRevB.105.104102](https://doi.org/10.1103/PhysRevB.105.104102)**I. INTRODUCTION**

Wave localization is a ubiquitous phenomenon in nature. Examples include the matter waves in atoms, light confined in droplets, and sound trapped in architectures. In periodic materials, we can easily judge whether the waves are localized or extended from the band structure. If the carrying frequency locates in the gap of the band structure, the waves are localized as bound states with no radiation to the outside environment. However, if the carrying frequency locates inside the continuous band region, the waves render as the extended states that propagate inside the periodic structure. In the study of different scattering materials where the waves propagate, there are several ways for realizing the wave localizations, including the Anderson localization in a disordered medium [1–7], defect states in flawed artificial crystals [8–11], topologically protected states in topological insulators [12–19], bound states in the continuum (BIC) [20–27], and others [28–30]. The Anderson localization stems from the wave interference among multiple scattering paths and is closely related to the disorder of scatterers. In the limit of strong scattering, waves can be completely localized inside the disordered material. Different from the Anderson localization, the defect states exist due to the presence of defects in imperfect artificial crystals. Typically, the defect states are located in the band gaps and localized at the defects inside the artificial crystals. Besides these, the topologically protected localized states, such as the zero-dimensional corner states in high-ordered topological insulators and two-dimensional (2D) drumhead states in Weyl semimetals, are also generated in nontrivial

band gaps. They are featured with robustness against the disorder in topological insulators and are finely localized at topologically protected positions. Recently, research on the topological skin effect has gained much attention [17–19], for which all the eigenmodes show strong field localizations on the edges/surfaces. It also needs to be mentioned that the BIC can realize perfect wave localization. The concept of BIC is contrary to conventional wisdom, since the localized modes coexist with the extended states in the continuous band of the system, rendering a perfect localization with zero radiation.

In this work, we theoretically and experimentally investigate the localization and delocalization of the flat-band bound states in a three-dimensional (3D) acoustic cubic lattice. Starting from the tight-binding approximation, we calculate the band structure of the designed cubic lattice with four sites per one unit cell, which consists of two dispersive bands and two degenerate flat bands. The flat-band energy is related to the on-site potentials. For a realizable acoustic cubic lattice comprising spherical cavities, as shown in Fig. 1(a), the flat-band frequency is inversely proportional to the cavity size. We first give the method of how to construct the flat-band states. From theoretical analyses, we prove that the flat-band states only depend on the excitation pressures and the coupling coefficients, which are frequency independent. Next, we study the localization and delocalization of flat-band states in the designed cubic acoustic lattice. On the flat-band state excitation, where the excitation frequency deviates from the flat-band frequency of the lattice, the sound wave can be perfectly localized in any primitive cell of the cubic lattice. However, when the excitation frequency hits the flat-band frequency, the flat-band state becomes a diffusive one, which can spread into the whole lattice due to the resonance energy transfer among primitive cells. It should be emphasized that

*Corresponding author: ygpeng@hust.edu.cn†Corresponding author: xfzhu@hust.edu.cn

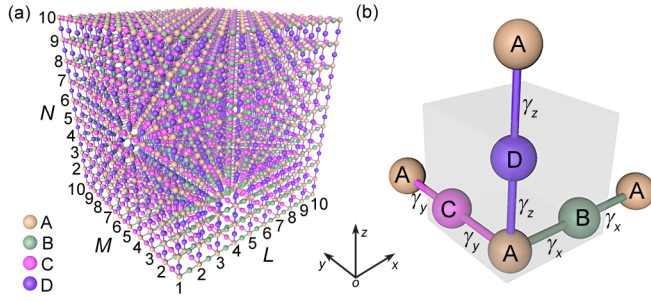


FIG. 1. (a) A schematic of the designed cubic lattice, where A, B, C, and D denote four types of sites that constitute four cubic sublattices. L , M , and N are the numbers of unit cells along x , y , and z directions, respectively. (b) A schematic of one unit cell, where the coupling coefficients between adjacent sites of A-B, A-C, and A-D are γ_x , γ_y , and γ_z , respectively.

the localization of flat-band bound states herein stems from the zero-value group velocities [31–35]. Last but not least, we provide the simulations and experimental demonstrations of the dispersive bulk states, flat-band bound states, and flat-band diffusive states in the designed cubic acoustic lattice. Furthermore, we show the localization of various composite flat-band bound states by superposing the elementary flat-band states in multiple primitive cells.

This work is formalized as follows. In Sec. II, we establish the tight-binding model of the designed cubic lattice.

II. MODEL AND DISCUSSIONS

Figure 1(a) shows a schematic of the designed cubic lattice, where the different colored spheres labeled by the letters A, B, C, and D denote four different types of sites. The variables L , M , and N denote the numbers of unit cells in the x , y , and z directions, respectively. Since there are four sites per one unit cell, the cubic lattice can be divided into four cubic sublattices as labeled by different colored spheres. Figure 1(b) shows the schematic of one unit cell, where the symbols γ_x , γ_y , and γ_z denote the coupling coefficients between the adjacent sites of A-B, A-C, and A-D, respectively.

Without losing the generality, we assume that the lattice constant of the designed cubic lattice is unitary, viz., $a = 1$. In the Wannier-state representation and with the assumption of evanescent couplings, the bulk Hamiltonian of the tight-binding cubic lattice can be expressed as [36,37]

$$\begin{aligned}
 H = & \sum_{l,m,n} \sum_{\alpha} [\varepsilon_{\alpha} |(l, m, n), \alpha\rangle \langle (l, m, n), \alpha| + \sum_{l,m,n} \{ \gamma_x [| (l, m, n), B\rangle \langle (l, m, n), A| + |(l+1, m, n), A\rangle \langle (l, m, n), B| \\
 & + \gamma_y [| (l, m, n), C\rangle \langle (l, m, n), A| + |(l, m+1, n), A\rangle \langle (l, m, n), C| + \gamma_z [| (l, m, n), D\rangle \langle (l, m, n), A| \\
 & + |(l, m, n+1), A\rangle \langle (l, m, n), D|] + \text{H.c.} \}, \quad (1)
 \end{aligned}$$

where H.c. stands for the Hermitian conjugate, ε_{α} denotes the on-site potential, and $|(l, m, n), \alpha\rangle$ denotes the Wannier state of the designed cubic lattice that localizes at the site α in the unit cell (l, m, n) , with $\alpha \in \{A, B, C, D\}$, $l \in \{1, 2, \dots, L\}$, $m \in \{1, 2, \dots, M\}$, and $n \in \{1, 2, \dots, N\}$. If the on-site potentials $\varepsilon_A = \varepsilon_B = \varepsilon_C = \varepsilon_D = \varepsilon_0$, and the wave number $k = \sqrt{k_x^2 + k_y^2 + k_z^2}$ in the Bloch representation, the bulk momentum-space Hamiltonian of the system can be expressed as

$$H(k) = \begin{pmatrix} \varepsilon_0 & \gamma_x(1 + e^{-ik_x}) & \gamma_y(1 + e^{-ik_y}) & \gamma_z(1 + e^{-ik_z}) \\ \gamma_x(1 + e^{ik_x}) & \varepsilon_0 & 0 & 0 \\ \gamma_y(1 + e^{ik_y}) & 0 & \varepsilon_0 & 0 \\ \gamma_z(1 + e^{ik_z}) & 0 & 0 & \varepsilon_0 \end{pmatrix}. \quad (2)$$

In Appendix A, we give the derivation of the bulk momentum-space Hamiltonian $H(k)$. By solving the eigenvalue problem with the Hamiltonian in Eq. (2), the quasienergy band structure or dispersion spectrum of the designed cubic lattice at any wave number k (with the bands indexed by 1 to 4) can be obtained as

$$E_1(k) = \varepsilon_0 - \varepsilon, \quad E_2(k) = E_3(k) = \varepsilon_0, \quad E_4(k) = \varepsilon_0 + \varepsilon, \quad (3)$$

where $\varepsilon = \sqrt{2\gamma_x^2(1 + \cos k_x) + 2\gamma_y^2(1 + \cos k_y) + 2\gamma_z^2(1 + \cos k_z)}$. The corresponding band vectors with the wave number k are

$$\begin{aligned}
 |u_1(k)\rangle &= \frac{1}{\sqrt{2}} \left(-1, \frac{\gamma_x(1 + e^{ik_x})}{\varepsilon}, \frac{\gamma_y(1 + e^{ik_y})}{\varepsilon}, \frac{\gamma_z(1 + e^{ik_z})}{\varepsilon} \right), & |u_2(k)\rangle &= \left(0, 1, 0, -\frac{\gamma_x(1 + e^{-ik_x})}{\gamma_z(1 + e^{-ik_z})} \right), \\
 |u_3(k)\rangle &= \left(0, 0, 1, -\frac{\gamma_y(1 + e^{-ik_y})}{\gamma_z(1 + e^{-ik_z})} \right), & |u_4(k)\rangle &= \frac{1}{\sqrt{2}} \left(1, \frac{\gamma_x(1 + e^{ik_x})}{\varepsilon}, \frac{\gamma_y(1 + e^{ik_y})}{\varepsilon}, \frac{\gamma_z(1 + e^{ik_z})}{\varepsilon} \right). \quad (4)
 \end{aligned}$$

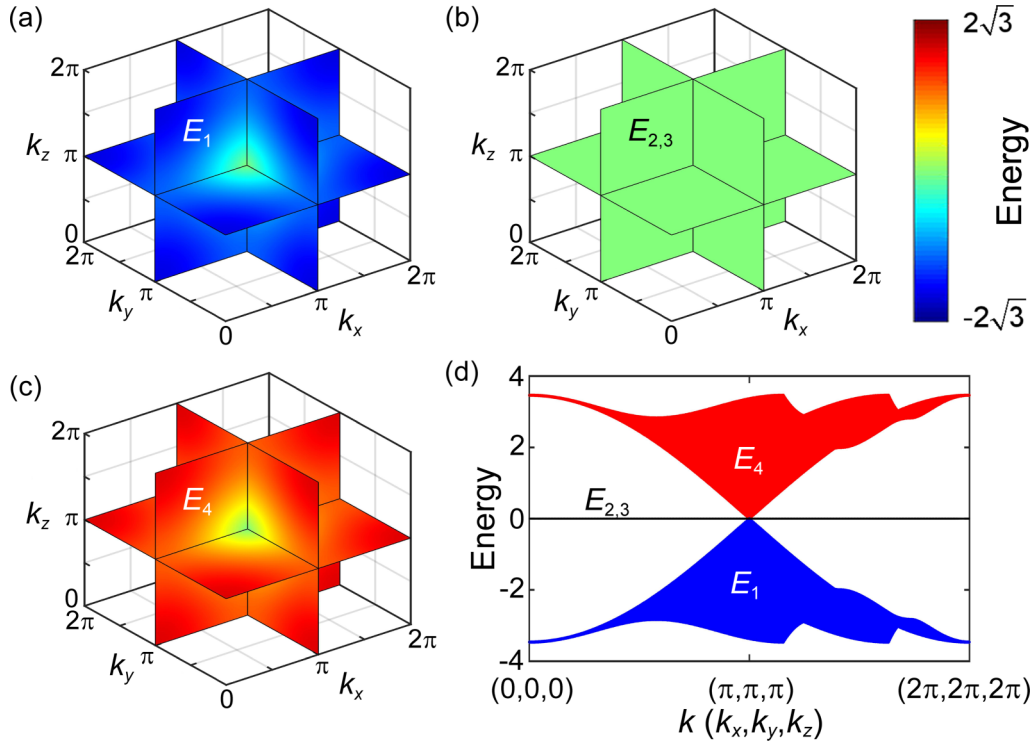


FIG. 2. (a)–(c) Dispersion relations of the quasienergy bands E_1 , $E_{2,3}$, and E_4 , respectively, where the wave number is in the first Brillouin zone $\{k_x, k_y, k_z\} = 0 \rightarrow 2\pi$. (d) Dispersion relations of the quasienergy bands E_1 , $E_{2,3}$, and E_4 with the wave vector $\mathbf{k} = (k_x, k_y, k_z)$ changing from $(0, 0, 0)$ to $(2\pi, 2\pi, 2\pi)$.

Equation (3) shows that the designed cubic lattice has two dispersive bands (E_1 , E_4) and two flat bands (E_2 , E_3). The two dispersive bands have the mirror symmetry with respect to the baseline of energy ε_0 . Figures 2(a)–2(c) show the dispersion relations of E_1 , $E_{2,3}$, and E_4 for the wave-number components in the 3D Brillouin zone ranging $\{k_x, k_y, k_z\} = 0 \rightarrow 2\pi$. In the numerical calculations, the designed cubic lattice is set to be isotropic with the intersite coupling coefficients $\gamma_x = \gamma_y = \gamma_z = 1$ and the on-site potential $\varepsilon_0 = 0$. Figure 2(d) shows the quasienergy bands of E_1 , $E_{2,3}$, and E_4 , where the wave vector $\mathbf{k} = (k_x, k_y, k_z)$ spans in the Brillouin zone from $(0, 0, 0)$ to $(2\pi, 2\pi, 2\pi)$. From Fig. 2(d), one can observe that the bands $E_{2,3}$ are perfectly flat. At the point of (π, π, π) , all the bands degenerate to generate a Weyl point.

In the following, we show how to construct the flat-band states in the designed cubic lattice. As a concrete example, we choose one primitive cell from the cubic lattice as shown in Fig. 3(a), where there are eight sites A at the corners of the primitive cell and four sites B, four sites C, and four sites D on the edges. The unit cell with the sites A_1 , B_1 , C_1 , and D_1 is indexed by (l_0, m_0, n_0) . In the chosen primitive cell, we assume that all the same sites have the same excitation sound pressures and are denoted by p_A , p_B , p_C , and p_D , respectively. Under this excitation condition, the initial excitation state can be expressed as

$$|\psi_0\rangle = \frac{1}{\sqrt{\mathcal{N}}} \sum_{\mathbf{k}} e^{-i\varphi} [p_A(1 + e^{-ik_x} + e^{-ik_x - ik_y} + e^{-ik_y} + e^{-ik_z} + e^{-ik_x - ik_z} + e^{-ik_x - ik_y - ik_z} + e^{-ik_y - ik_z})|\mathbf{k}\rangle \otimes |\mathbf{A}\rangle + p_B(1 + e^{-ik_z} + e^{-ik_y - ik_z} + e^{-ik_y})|\mathbf{k}\rangle \otimes |\mathbf{B}\rangle$$

$$+ p_C(1 + e^{-ik_x} + e^{-ik_x - ik_z} + e^{-ik_z})|\mathbf{k}\rangle \otimes |\mathbf{C}\rangle + p_D(1 + e^{-ik_x} + e^{-ik_x - ik_y} + e^{-ik_y})|\mathbf{k}\rangle \otimes |\mathbf{D}\rangle], \quad (5)$$

where the phase $\varphi = l_0 k_x + m_0 k_y + n_0 k_z$. The details about the derivation process of the initial excitation state $|\psi_0\rangle$ in Eq. (5) are shown in Appendix B. At any given wave number \mathbf{k} , by projecting Eq. (5) into the band-vector basis $\{u_1(\mathbf{k}), u_2(\mathbf{k}), u_3(\mathbf{k}), u_4(\mathbf{k})\}$, the initial excitation state $|\psi_0\rangle$ can be expressed as $|\psi_0\rangle = \sum_n c_n u_n(\mathbf{k})$, where c_n represents the occupation probability of the band vector $u_n(\mathbf{k})$. According to Eqs. (4) and (5) and the condition of $p_A = 0$, the occupation probabilities of the dispersive band vectors $u_1(\mathbf{k})$ and $u_4(\mathbf{k})$ are

$$c_{1,4} = \frac{(1 + e^{-ik_x})(1 + e^{-ik_y})(1 + e^{-ik_z})}{\sqrt{2}\varepsilon} (p_B \gamma_x + p_C \gamma_y + p_D \gamma_z). \quad (6)$$

From Eq. (6), we can clearly see that the occupation probabilities $c_{1,4}$ are determined by the excitation sound pressures p_B , p_C , and p_D and the intersite coupling coefficients γ_x , γ_y , and γ_z . For example, when the excitation sound pressures satisfy the relation of $p_D \gamma_z = -(p_B \gamma_x + p_C \gamma_y)$, we can obtain the occupation probabilities $c_{1,4} = 0$. Thus, under this excitation condition, the initial excitation state $|\psi_0\rangle$ only occupies the flat-band states of the designed cubic lattice and can be written as $|\psi_0\rangle = c_2 u_2(\mathbf{k}) + c_3 u_3(\mathbf{k})$. Since the group velocities of flat bands E_2 and E_3 equal to zero, the initial excitation state $|\psi_0\rangle$ is thus a flat-band bound state that is localized in the excited primitive cell, except for the special case of resonance energy transfer, which will be discussed

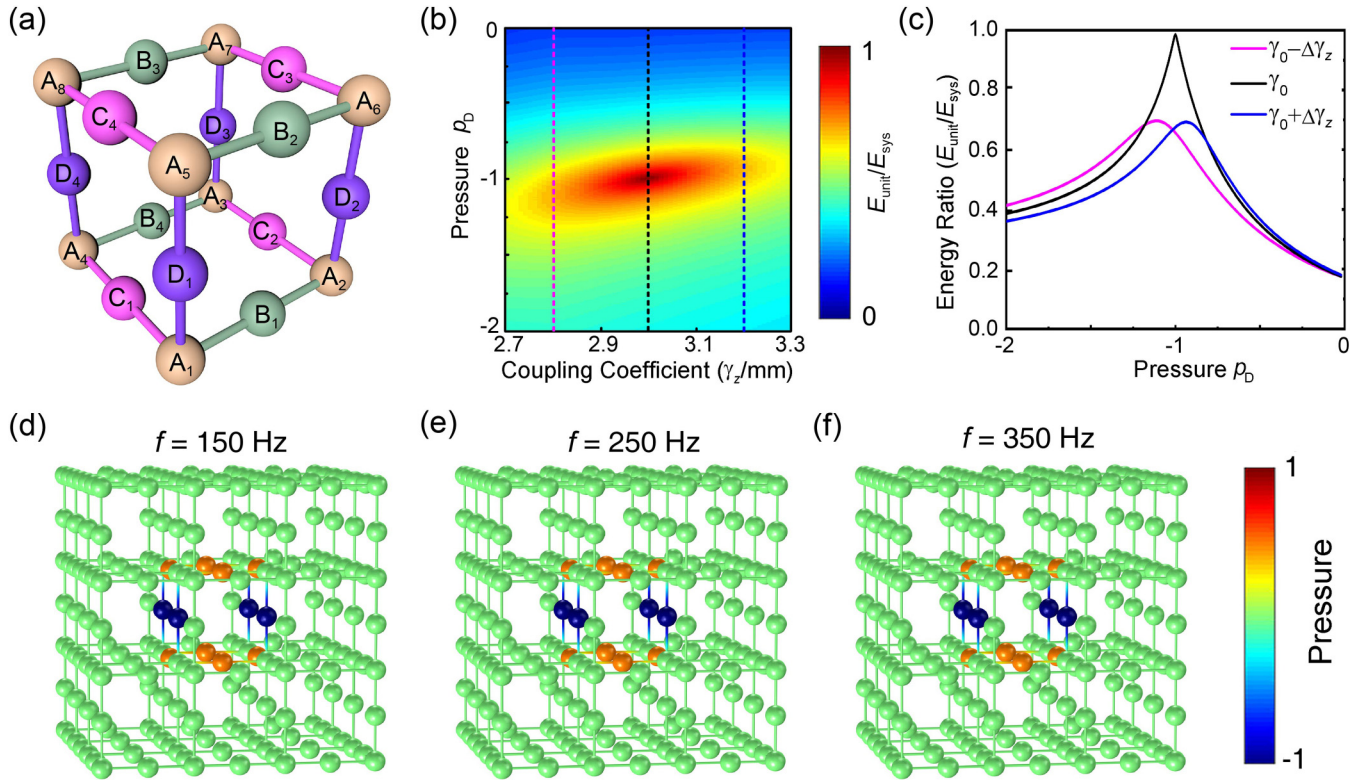


FIG. 3. (a) A schematic of one primitive cell with site indices. (b) The changing relation of the energy ratio $E_{\text{unit}}/E_{\text{sys}}$ versus the excitation pressure p_D and the coupling coefficient γ_z , where E_{unit} denotes the energy localized in the excited primitive cell and E_{sys} denotes the energy in the whole system. (c) The relation of the energy ratio $E_{\text{unit}}/E_{\text{sys}}$ to the excitation pressure p_D , where the black line, the magenta line, and the blue line correspond to the cases of $\gamma_z = 2.8, 3.0,$ and 3.2 mm, respectively. (d)–(f) Simulation results of the flat-band bound states at the different excitation frequencies of 150, 250, and 350 Hz.

later. As we know, for a periodic lattice system with \mathcal{N} unit cells, there exist \mathcal{N} wave numbers in the first Brillouin zone. Thus, for the designed cubic lattice with \mathcal{N} unit cells, it should be $2\mathcal{N}$ flat-band states due to the fact that there are two flat-band states for a given wave number k . Figure 3(b) shows the relation of the energy ratio $E_{\text{unit}}/E_{\text{sys}}$ versus the excitation pressure p_D and the intersite coupling coefficient γ_z , where E_{unit} denotes the acoustic energy localized in the excited primitive cell and E_{sys} denotes the total energy in the system. In the designed cubic lattice, the intersite coupling coefficient γ_α can be tuned by changing the radius r_α of the coupling tube with a fixed length, where $\alpha = x, y, z$. Because the radius of the coupling tube is directly related to the intersite coupling coefficient, here we use the radius r_α to represent the coupling coefficient γ_α for simplicity in the following. In the full-wave simulation, the cubic lattice consists of $10 \times 10 \times 10$ unit cells. All the spherical cavities are identical with the radius $r = 25$ mm. All the coupling tubes have the same length of $l = 60$ mm. The intersite coupling coefficients are $\gamma_x = \gamma_y = 3$ mm and $\gamma_z \in [2.7, 3.3]$ mm. In the excited primitive cell, the excitation sound pressures are set to be $p_B = p_C = 1/2$ and $p_D \in [-2, 0]$ (in an arbitrary unit). The excitation frequency $f = 150$ Hz. From Fig. 3(b), we find that the energy ratio $E_{\text{unit}}/E_{\text{sys}}$ reaches unity at a singularity point. Figure 3(c) quantitatively shows the changes of energy ratio $E_{\text{unit}}/E_{\text{sys}}$ with respect to the excitation pressure p_D . The results show that the singularity point occurs in the isotropic cubic lattice, where the coupling coefficients $\gamma_x = \gamma_y = \gamma_z$

and the excitation pressure $p_D = -1$, in agreement with the theoretical analysis. Additionally, it indicates the existence of flat-band bound states. From Eq. (6), we can know that the generations of flat-band states are only related to the excitation sound pressures and coupling coefficients, which are frequency independent. In Figs. 3(d)–3(f), we verify the perfect localizations of flat-band states at different frequencies of 150, 250, and 350 Hz. In numerical simulations, the cubic lattice consists of $4 \times 4 \times 4$ unit cells. All the spherical cavities are identical with the radius $r = 25$ mm. All the coupling channels have the same radius of $r_x = r_y = r_z = 3$ mm and the length of $l = 60$ mm. The excitation pressures are set to be $p_A = 0, p_B = p_C = 1/2,$ and $p_D = -1$ in the chosen primitive cell, which satisfies the condition of flat-band state excitation.

Under the same flat-band state excitation and by changing the excitation frequency, we find that the flat-band state is not always localized in the chosen primitive cell. In Fig. 4, we show the delocalization of flat-band states. Figure 4(a) shows the changing relation of the energy ratio $E_{\text{unit}}/E_{\text{sys}}$ versus the sphere radius and excitation frequency. From Fig. 4(a), we can clearly see that the energy ratio $E_{\text{unit}}/E_{\text{sys}} \rightarrow 0$ at some specific excitation frequencies, which indicates the flat-band states are delocalized and spread into the whole cubic lattice. Besides that, we find that the delocalization frequency is inversely proportional to the sphere radius. A quantitative analysis of the energy ratio versus the excitation frequency is shown in Fig. 4(b), where the magenta line,

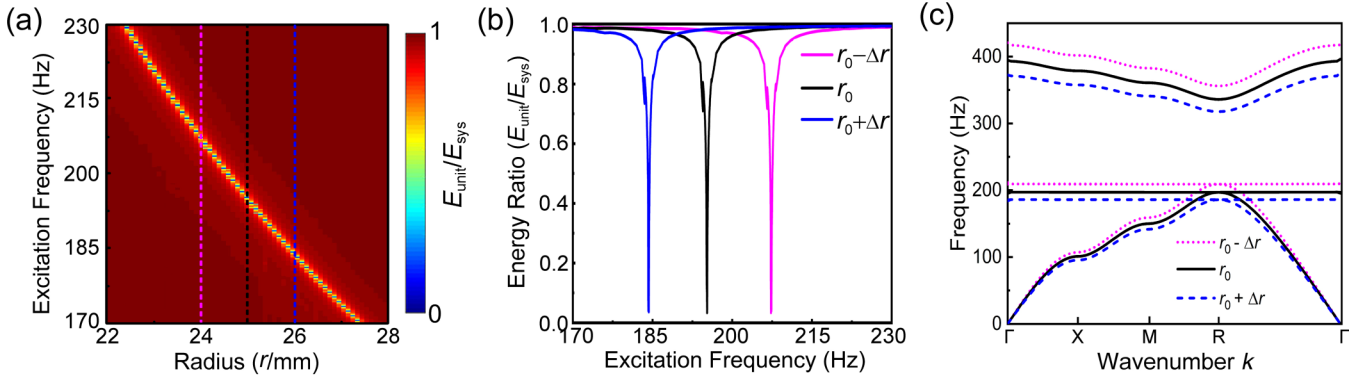


FIG. 4. (a) The energy ratio $E_{\text{unit}}/E_{\text{sys}}$ versus the sphere radius and the excitation frequency, where the cubic lattice is isotropic and the initial excitation state is a flat-band state. (b) A quantitative analysis of the energy ratio versus the excitation frequency, where the magenta line, the black line, and the blue line correspond to $r = 24, 25,$ and 26 mm, respectively. (c) The band structure of the designed cubic lattice along $\Gamma \rightarrow X \rightarrow M \rightarrow R \rightarrow \Gamma$ in the first Brillouin zone. In the simulation, the cubic lattice is isotropic with the sphere radius being $r = 24, 25,$ and 26 mm, respectively.

the black line, and the blue line correspond to the cases of $r = 24, 25,$ and 26 mm, respectively. The singularity points of $E_{\text{unit}}/E_{\text{sys}} \rightarrow 0$ locate at around 184, 195, and 207 Hz for the three cases, with the full width at half maximum (FWHM) of dips being below 0.5 Hz, which correspond to the flat-band frequencies of designed cubic lattices in Fig. 4(c). In the band-structure calculations of Fig. 4(c), the wave number k only takes the values along $\Gamma \rightarrow X \rightarrow M \rightarrow R \rightarrow \Gamma$ in the first Brillouin zone. By comparing Fig. 4(c) with Fig. 2(d), the on-site potential of the cubic lattice is closely related to the sphere radius, where the finite size induces a band gap in Fig. 4(c). Thus, from Figs. 3 and 4, we find that, when the excitation frequency deviates from the flat-band frequency of the cubic lattice, the flat-band states are well localized in the chosen primitive cell. As shown in Figs. 3(d)–3(f), at the frequencies of 150, 250, and 350 Hz, the excited modes separately locate in the lower bulk band, the band gap, and the upper bulk band of the cubic lattice [the black line in Fig. 4(c)]. When the excitation frequency hits the flat-band frequency of the cubic lattice, the flat-band states are changed to be extensively spreading or diffusing in the cubic lattice due to the resonance energy transfer among primitive cells [38–40]. Featured with the ultrasensitivity to the wave frequency, the localization and delocalization of flat-band states are expected to have important applications in acoustic sensing and switching.

III. SIMULATION AND EXPERIMENTAL RESULTS

In this section, we show the simulation and experimental results of the sound wave propagation in the cubic lattices, where the spherical cavity radius $r = 25$ mm, the coupling tube radii $\gamma_x = \gamma_y = \gamma_z = 3$ mm, and the tube length $l = 60$ mm. In Fig. 5(a), we show the dispersive propagation of bulk mode, where the excitation is imposed in the center primitive cell with the excitation pressures $p_A = 0, p_B = p_C = 1/2,$ and $p_D = 1,$ and the excitation frequency $f = 150$ Hz. In this case, the acoustic wave is not localized, because the occupation probabilities of dispersive band vectors $u_1(k)$ and $u_4(k)$ are nonzero [$c_{1,4} \neq 0$ in Eq. (6)]. Similarly, according to

Eq. (6), we can construct a flat-band state on condition that the excitation sound pressures are $p_A = 0, p_B = p_C = -1/2,$ and $p_D = 1.$ Since the excitation frequency (150 Hz) is not equal to the flat-band frequency (≈ 195 Hz) of the designed cubic lattice, the flat-band state is a bound state that is completely localized in the center primitive cell, as shown in Fig. 5(b). It is worth noting that the flat-band bound state can be not only localized in the center primitive cell but also in any primitive cell of the cubic lattice. In Appendix C, we show the other types of flat-band bound states, which include 11 elementary flat-band bound states in one primitive cell and some composite flat-band bound states. When we set the excitation frequency (195 Hz) to be close to the flat-band frequency (≈ 195 Hz) of the designed cubic lattice, resonance energy transfer of the flat-band state will occur among multiple primitive cells. In this case, the flat-band state is actually a diffusive one. In Fig. 5(c), we show the delocalization of the flat-band state, where the acoustic energy is spreading into the whole cubic lattice. In addition, according to the theorem of superposition, we can construct a composite flat-band state by superposing two or more elementary flat-band states. It is the same for the case of elementary flat-band states, where we can analyze the localization and delocalization of the composite flat-band states by changing the excitation frequency. Figures 5(d) and 5(e) show the localization of the composite flat-band state. In Fig. 5(d), we give the schematic of two adjacent primitive cells, where each site is marked by a site index. Figure 5(e) shows that a composite flat-band bound state comprises two out-of-phase modes in Fig. 5(b), where the acoustic wave is effectively localized in the excited primitive cells. In full-wave simulations, the excitation sound pressures are set to be $p_A = 0$ for sites A, $p_{B_1} = p_{B_2} = p_{B_3} = p_{B_4} = 1/2$ and $p_{B_5} = p_{B_6} = p_{B_7} = p_{B_8} = -1/2$ for sites B, $p_{C_1} = p_{C_2} = 1/2, p_{C_3} = p_{C_4} = 0,$ and $p_{C_5} = p_{C_6} = -1/2$ for sites C, and $p_{D_1} = p_{D_2} = -1, p_{D_3} = p_{D_4} = 0,$ and $p_{D_5} = p_{D_6} = 1$ for sites D. The excitation frequency $f = 150$ Hz, which is different from the resonance frequency of the designed cubic lattice.

We further experimentally demonstrated the localization and delocalization of the flat-band states. The fabricated

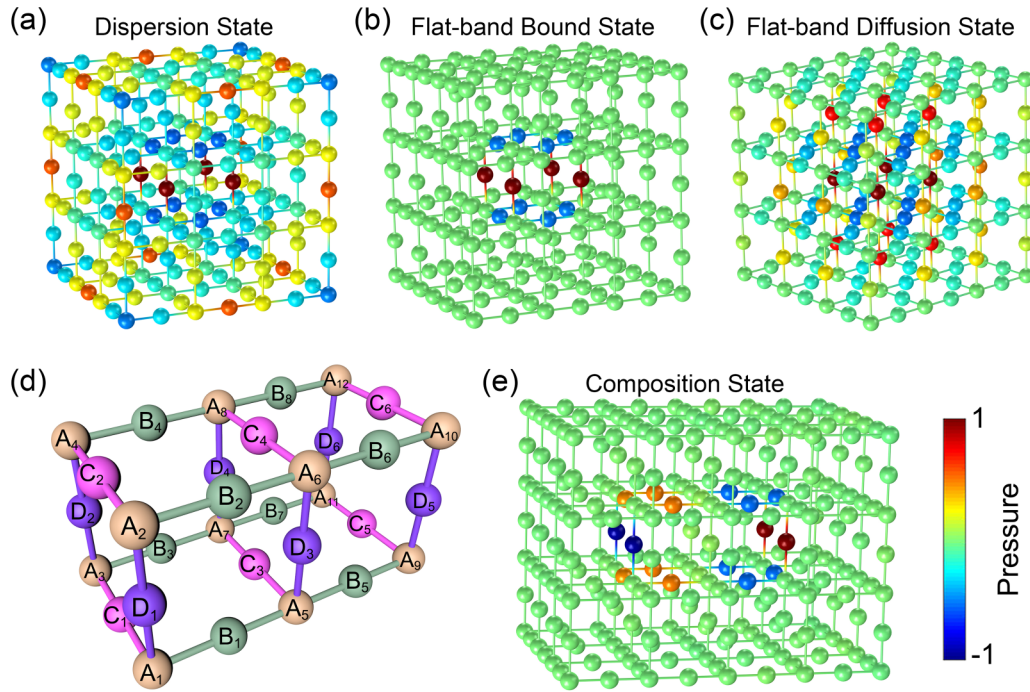


FIG. 5. The simulation results of the normalized sound pressure distributions for (a) the dispersive bulk state, (b) the flat-band bound state, and (c) the flat-band diffusion state. (d) A schematic of two adjacent primitive cells, where each site has a marked site index. (e) Normalized sound pressure distribution of the composite flat-band bound state, which is the superposition of two out-of-phase flat-band modes in (b).

sample of the designed cubic lattice is shown in Fig. 6(a), which has $4 \times 5 \times 4$ unit cells. The hollow aluminum alloy spheres were processed by the numerically controlled machine tools (accuracy ~ 0.05 mm). The inner diameter of the spherical cavity is 50 mm. The inner diameter and length of coupling tubes are 6 and 60 mm, respectively. The sample was anchored on the optical platform holder. In Fig. 6(b), we demonstrate the propagation of dispersive bulk mode in experiments, where we use the same excitation condition as the one in Fig. 5(a). In experiments, 12 speakers were placed in the selected spherical cavities and driven by the multifunctional signal generator (Tektronix AFG3022C) in phase. Besides that, we also used the power amplifiers (AOSIBAO A8 HIFI) to control the excitation sound pressures of the 12 speakers. Sound intensities in the spherical cavities were measured by inserting a microphone (1/8-in. Brüel & Kjær 4138-A-015) into the perforated holes. All the data were recorded by the Brüel & Kjær 3160-A-042 4-channel analyzer. The sampling time of data was set to be 1 s in the measurement. The frequency response was obtained with the fast Fourier transform analysis of Brüel & Kjær PULSE software LabShop. Figure 6(c) experimentally demonstrates the localization of flat-band state, where the excitation condition is the same as the case in Fig. 5(b). In this case, since the initial excitation state is a flat-band state and the excitation frequency deviates from the flat-band frequency of the lattice, the sound energy is perfectly localized in the excited primitive cell. Specifically, the measured sound intensities are $I_{B_1} = 85\,849$ mPa², $I_{B_2} = 66\,049$ mPa², $I_{B_3} = 62\,500$ mPa², $I_{B_4} = 76\,176$ mPa², $I_{B_6} = 61\,504$ mPa², $I_{B_7} = 78\,400$ mPa², $I_{B_8} = 72\,361$ mPa², $I_{C_1} = 64\,516$ mPa², $I_{C_2} = 81\,796$ mPa², $I_{C_3} = 66\,564$ mPa², $I_{C_4} = 56\,644$ mPa², $I_{D_1} = 294\,849$ mPa², $I_{D_2} = 266\,256$ mPa², $I_{D_3} = 274\,576$ mPa², and $I_{D_4} = 299\,209$ mPa²

in the excited primitive cell. The measured intensities in other sites are below 1000 mPa². The site indices can be referred to in Fig. 3(a). Under the same excitation in Fig. 6(c), we show the relation of E_{lkge} with respect to the excitation frequency in Fig. 6(d), where the red dots and the blue line represent the experiment and simulation results, respectively. Here, E_{lkge} denotes the normalized leaky energy from the excited primitive cell, which can be calculated by summing the intensities of all spherical cavities except for the ones in the excited cell. When the excitation frequency is 196 Hz, the leaky energy of the flat-band state reaches the maximum in experiments. The quality factor for the delocalization of the flat-band state is related to the FWHM of the leaky energy peak in Fig. 6(d). The measured and simulated FWHMs are about 10 and 0.5 Hz, respectively. It should be pointed out that, in experiments, the excitation frequency interval is 5 Hz in the ranges of 150–190 and 210–250 Hz, while the interval is 1 Hz in the range of 190–210 Hz for better characterizing the peak. With the flat-band excitation condition, we experimentally verified the delocalization of flat-band state by tuning the excitation frequency into 196 Hz, as shown in Fig. 6(e). The result shows that the normalized sound intensities are not localized in the excited cell but are spreading into the whole lattice. We experimentally verified the localization of the composite flat-band state in Fig. 6(f), where the normalized sound intensities are confined in the two adjacent cells. In this case, the measured sound intensities are $I_{B_1} = 77\,841$ mPa², $I_{B_2} = 74\,529$ mPa², $I_{B_3} = 73\,441$ mPa², $I_{B_4} = 63\,504$ mPa², $I_{B_5} = 76\,176$ mPa², $I_{B_6} = 61\,504$ mPa², $I_{B_7} = 78\,400$ mPa², $I_{B_8} = 72\,361$ mPa², $I_{C_1} = 64\,516$ mPa², $I_{C_2} = 81\,796$ mPa², $I_{C_3} = 66\,564$ mPa², $I_{C_4} = 56\,644$ mPa², $I_{D_1} = 294\,849$ mPa², $I_{D_2} = 266\,256$ mPa², $I_{D_3} = 274\,576$ mPa², and $I_{D_4} = 299\,209$ mPa²

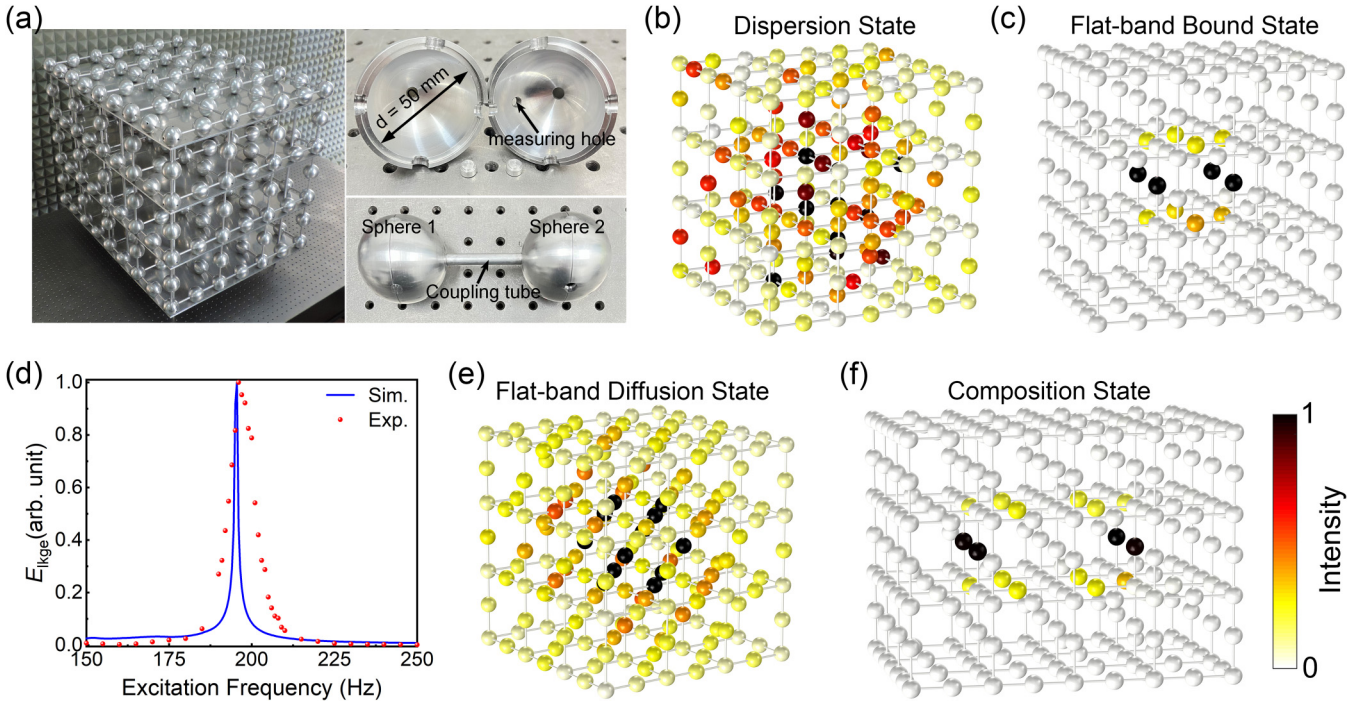


FIG. 6. (a) The fabricated sample. (b) The measured sound intensity distribution of the dispersive bulk state. (c) The measured sound intensity distribution of a flat-band bound state. (d) The relation of the normalized leaky energy E_{lkge} with respect to the change of excitation frequencies. The red dots and blue line represent the experiment and simulation results, respectively. (e) The measured sound intensity distribution of a flat-band diffusive state. (f) The measured sound intensity distribution of a composite flat-band bound state. All the experimental results are normalized.

in the excited cells. The measured intensities in other sites are below 1000 mPa^2 . The site indices can be referred to in Fig. 5(d). Here the excitation condition in Fig. 6(f) is the same as the one in Fig. 5(e). In Appendix C, we also experimentally demonstrate the localization of other complicated composite flat-band states.

IV. CONCLUSIONS

In conclusion, we theoretically and experimentally investigate the localization and delocalization of the flat-band states in the designed cubic lattice with four sites per one unit cell. The flat-band states can be realized by setting the excitation sound pressures and the coupling coefficients, which are frequency independent. Under the flat-band state excitation, the sound wave can be either localized or delocalized, which is determined by the excitation frequency. When the excitation frequency hits the flat-band frequency of the cubic lattice, the flat-band state is spreading into the whole cubic lattice due to the resonance energy transfer among primitive cells. When the excitation frequency is tuned to deviate from the flat-band frequency, the flat-band state can be perfectly localized in any primitive cell of the cubic lattice. Moreover, we demonstrate more complicated flat-band bound states by superposing different elementary flat-band bound states in multiple primitive cells. Comparing with the Anderson localization, the construction of the flat-band bound state does not need the introduction of disorder into the periodic cubic lattice. Also, different from the defect states and the topologically protected states, the excitation frequency of the flat-band bound state is

not limited to a finite range, which takes the values both in band gaps and in continuous bulk bands of the lattice. If the excitation frequency of the flat-band bound state locates inside the bulk band, it can be regarded as a BIC-like state. However, in this case, the realization of the BIC-like state requires that the excitation frequency deviates from the frequency of flat-band state of the lattice. Our results shed light on the wave dynamics of higher dimensional bound states, which provides a unique scheme for controlling sound in 3D networks and could be useful for realizing new functionalities and cavity designs based on 3D BICs.

ACKNOWLEDGMENTS

This work was supported by National Natural Science Foundation of China (Grants No. 11690030 and No. 11690032). X.-F.Z. would like to acknowledge the financial support from the Bird Nest Plan of HUST.

APPENDIX A: DERIVATION OF BULK MOMENTUM-SPACE HAMILTONIAN

As discussed in the Sec. II, the tight-binding bulk Hamiltonian of the designed cubic lattice can be expressed as Eq. (1) in the Wannier-state representation. Meanwhile, based on the theorem of tensor products, the Wannier state can also be expressed as $|l, m, n, \alpha\rangle = |l, m, n\rangle \otimes |\alpha\rangle \in \mathcal{H}_{\text{external}} \otimes \mathcal{H}_{\text{internal}}$. Under such tensor representation, the internal degrees of the lattice are separated from the external one. Thus,

the systematic bulk Hamiltonian Eq. (1) becomes

$$\begin{aligned}
H = & \sum_{l,m,n} \sum_{\alpha} [\varepsilon_{\alpha} |l, m, n\rangle \langle l, m, n| \otimes |\alpha\rangle \langle \alpha|] + \sum_{l,m,n} [\gamma_x (|l, m, n\rangle \langle l, m, n| \otimes |B\rangle \langle A| + |l+1, m, n\rangle \langle l, m, n| \otimes |A\rangle \langle B|) \\
& + \gamma_y (|l, m, n\rangle \langle l, m, n| \otimes |C\rangle \langle A| + |l, m+1, n\rangle \langle l, m, n| \otimes |A\rangle \langle C|) \\
& + \gamma_z (|l, m, n\rangle \langle l, m, n| \otimes |D\rangle \langle A| + |l, m, n+1\rangle \langle l, m, n| \otimes |A\rangle \langle D|) + \text{H.c.}]. \tag{A1}
\end{aligned}$$

By performing the Fourier transform to the external degree of freedom of the lattice, we have

$$|k\rangle = \frac{1}{\sqrt{\mathcal{N}}} \sum_{l,m,n} e^{i(lk_x + mk_y + nk_z)} |l, m, n\rangle. \tag{A2}$$

By plugging Eq. (A2) into Eq. (A1), we can thus obtain the bulk momentum-space Hamiltonian $H(k)$ as

$$\begin{aligned}
H(k) = & \langle k | H | k \rangle \\
= & \frac{1}{\sqrt{\mathcal{N}}} \sum_{l',m',n'} e^{-i(l'k_x + m'k_y + n'k_z)} \langle l', m', n' | \left\{ \sum_{l,m,n} \sum_{\alpha} (\varepsilon_{\alpha} |l, m, n\rangle \langle l, m, n| \otimes |\alpha\rangle \langle \alpha|) + \sum_{l,m,n} [\gamma_x (|l, m, n\rangle \langle l, m, n| \otimes |B\rangle \langle A| + |l+1, m, n\rangle \langle l, m, n| \otimes |A\rangle \langle B|) \right. \\
& + \gamma_y (|l, m, n\rangle \langle l, m, n| \otimes |C\rangle \langle A| + |l, m+1, n\rangle \langle l, m, n| \otimes |A\rangle \langle C|) \\
& \left. + \gamma_z (|l, m, n\rangle \langle l, m, n| \otimes |D\rangle \langle A| + |l, m, n+1\rangle \langle l, m, n| \otimes |A\rangle \langle D|) + \text{H.c.} \right\} \frac{1}{\sqrt{\mathcal{N}}} \sum_{l'',m'',n''} e^{i(l''k_x + m''k_y + n''k_z)} |l'', m'', n''\rangle \\
= & \sum_{\alpha} \varepsilon_{\alpha} |\alpha\rangle \langle \alpha| + \gamma_x (|A\rangle \langle B| + e^{-ik_x} |A\rangle \langle B| + |B\rangle \langle A| + e^{ik_x} |B\rangle \langle A|) + \gamma_y (|A\rangle \langle C| + e^{ik_y} |A\rangle \langle C| + |C\rangle \langle A| + e^{-ik_y} |C\rangle \langle A|) \\
& + \gamma_z (|A\rangle \langle D| + e^{ik_z} |A\rangle \langle D| + |D\rangle \langle A| + e^{-ik_z} |D\rangle \langle A|). \tag{A3}
\end{aligned}$$

From Eq. (A3), we know that, under the basis states $\{|A\rangle, |B\rangle, |C\rangle, |D\rangle\}$ with the given wave number k , the bulk momentum-space Hamiltonian of the lattice can be expressed in a 4×4 matrix of

$$H(k) = \begin{pmatrix} \varepsilon_A & \gamma_x(1 + e^{-ik_x}) & \gamma_y(1 + e^{-ik_y}) & \gamma_z(1 + e^{-ik_z}) \\ \gamma_x(1 + e^{ik_x}) & \varepsilon_B & 0 & 0 \\ \gamma_y(1 + e^{ik_y}) & 0 & \varepsilon_C & 0 \\ \gamma_z(1 + e^{ik_z}) & 0 & 0 & \varepsilon_D \end{pmatrix}. \tag{A4}$$

APPENDIX B: CONSTRUCTION OF THE FLAT-BAND STATES

From Appendix A, we conclude that the Hamiltonian of the cubic lattice system can be expressed by either the real/Wannier representation or the momentum/Bloch representation. In the same way, the transient state function $|\psi\rangle$ of the system can be separately expanded by the basic states $|l, m, n\rangle \otimes |\alpha\rangle$ and $|k\rangle \otimes |\alpha\rangle$ in both Wannier representation and Bloch representation.

$$|\psi\rangle = \sum_{lmn,\alpha} C_{lmn,\alpha} |l, m, n\rangle \otimes |\alpha\rangle, \tag{B1a}$$

$$|\psi\rangle = \sum_{k,\alpha} C_{k,\alpha} |k\rangle \otimes |\alpha\rangle, \tag{B1b}$$

where $C_{lmn,\alpha}$ and $C_{k,\alpha}$ are the occupation probabilities of the Wannier states $|l, m, n\rangle \otimes |\alpha\rangle$ and the Bloch states $|k\rangle \otimes |\alpha\rangle$, respectively. For example, when the site A_1 in Fig. 3(a) is excited by the sound pressure p_{A_1} , the excitation state $|\psi_{A_1}\rangle$ can be expressed under the Wannier representation as

$$|\psi_{A_1}\rangle = p_{A_1} |l_0, m_0, n_0\rangle \otimes |A\rangle. \tag{B2}$$

However, for the Bloch representation, according to the Fourier transform of $|l_0, m_0, n_0\rangle = \mathcal{N}^{-1/2} \sum_k e^{-i(l_0k_x + m_0k_y + n_0k_z)} |k\rangle$, the excitation state $|\psi_{A_1}\rangle$ is

$$|\psi_{A_1}\rangle = \frac{1}{\sqrt{\mathcal{N}}} \sum_k p_{A_1} e^{-i(l_0k_x + m_0k_y + n_0k_z)} |k\rangle \otimes |A\rangle, \tag{B3}$$

where the unit-cell index of site A_1 is (l_0, m_0, n_0) . From Eq. (B3), when the site A_2 in Fig. 3(a) is excited by the acoustic pressure p_{A_2} , the excitation state $|\psi_{A_2}\rangle$ can be expressed as

$$|\psi_{A_2}\rangle = \frac{1}{\sqrt{\mathcal{N}}} \sum_k p_{A_2} e^{-i[(l_0+1)k_x + m_0k_y + n_0k_z]} |k\rangle \otimes |A\rangle, \tag{B4}$$

where the unit-cell index of site A_2 is $(l_0 + 1, m_0, n_0)$. Since sites A_1 and A_2 have the different unit-cell indices, the excitation state $|\psi_{A_2}\rangle$ thus has an additional phase factor e^{-ik_x} in comparison to the excitation state $|\psi_{A_1}\rangle$. Similarly, we can obtain the excitation states at other sites in turn. When all the sites in Fig. 3(a) are excited simultaneously, the excitation

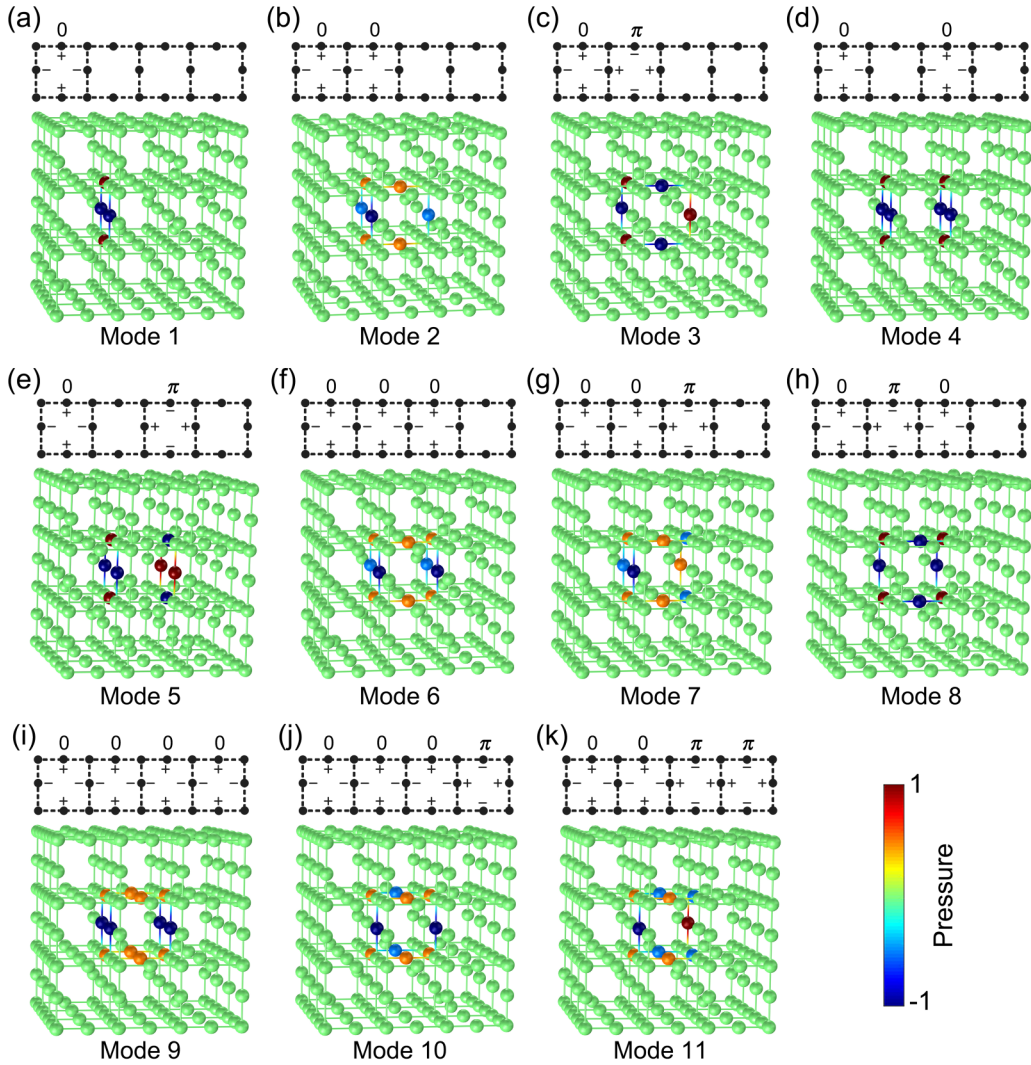


FIG. 7. The simulations on elementary flat-band bound states, where the sound pressures are normalized with respect to their maxima, respectively.

state $|\psi_0\rangle$ can be expressed as

$$\begin{aligned}
 |\psi_0\rangle = & \frac{1}{\sqrt{\mathcal{N}}} \sum_k e^{-i\varphi} [(p_{A_1} + p_{A_2} e^{-ik_x} + p_{A_3} e^{-ik_x - ik_y} + p_{A_4} e^{-ik_y})|k\rangle \otimes |A\rangle + (p_{A_5} e^{-ik_z} + p_{A_6} e^{-ik_x - ik_z} \\
 & + p_{A_7} e^{-ik_x - ik_y - ik_z} + p_{A_8} e^{-ik_y - ik_z})|k\rangle \otimes |A\rangle + (p_{B_1} + p_{B_2} e^{-ik_z} + p_{B_3} e^{-ik_y - ik_z} + p_{B_4} e^{-ik_y})|k\rangle \otimes |B\rangle \\
 & + (p_{C_1} + p_{C_2} e^{-ik_x} + p_{C_3} e^{-ik_x - ik_z} + p_{C_4} e^{-ik_z})|k\rangle \otimes |C\rangle + (p_{D_1} + p_{D_2} e^{-ik_x} + p_{D_3} e^{-ik_x - ik_y} + p_{D_4} e^{-ik_y})|k\rangle \otimes |D\rangle], \quad (\text{B5})
 \end{aligned}$$

where the phase $\varphi = l_0 k_x + m_0 k_y + n_0 k_z$.

From Eq. (B5), to construct a flat-band state, we assume that the excitation sound pressures $p_{A_1} = p_{A_2} = p_{A_3} = p_{A_4} = p_{A_5} = p_{A_6} = p_{A_7} = p_{A_8} = 0$ for the A sites, $p_{B_1} = p_{B_2} = p_{B_3} = p_{B_4} = p_B$ for the B sites, $p_{C_1} = p_{C_2} = p_{C_3} = p_{C_4} = p_C$ for the C sites, and $p_{D_1} = p_{D_2} = p_{D_3} = p_{D_4} = p_D$ for the D sites. Finally, the excitation state $|\psi_0\rangle$ in Eq. (B5) is simplified to

$$\begin{aligned}
 |\psi_0\rangle = & \frac{1}{\sqrt{\mathcal{N}}} \sum_k e^{-i\varphi} [p_B(1 + e^{-ik_y})(1 + e^{-ik_z})|k\rangle \otimes |B\rangle + p_C(1 + e^{-ik_x})(1 + e^{-ik_z})|k\rangle \otimes |C\rangle \\
 & + p_D(1 + e^{-ik_x})(1 + e^{-ik_y})|k\rangle \otimes |D\rangle]. \quad (\text{B6})
 \end{aligned}$$

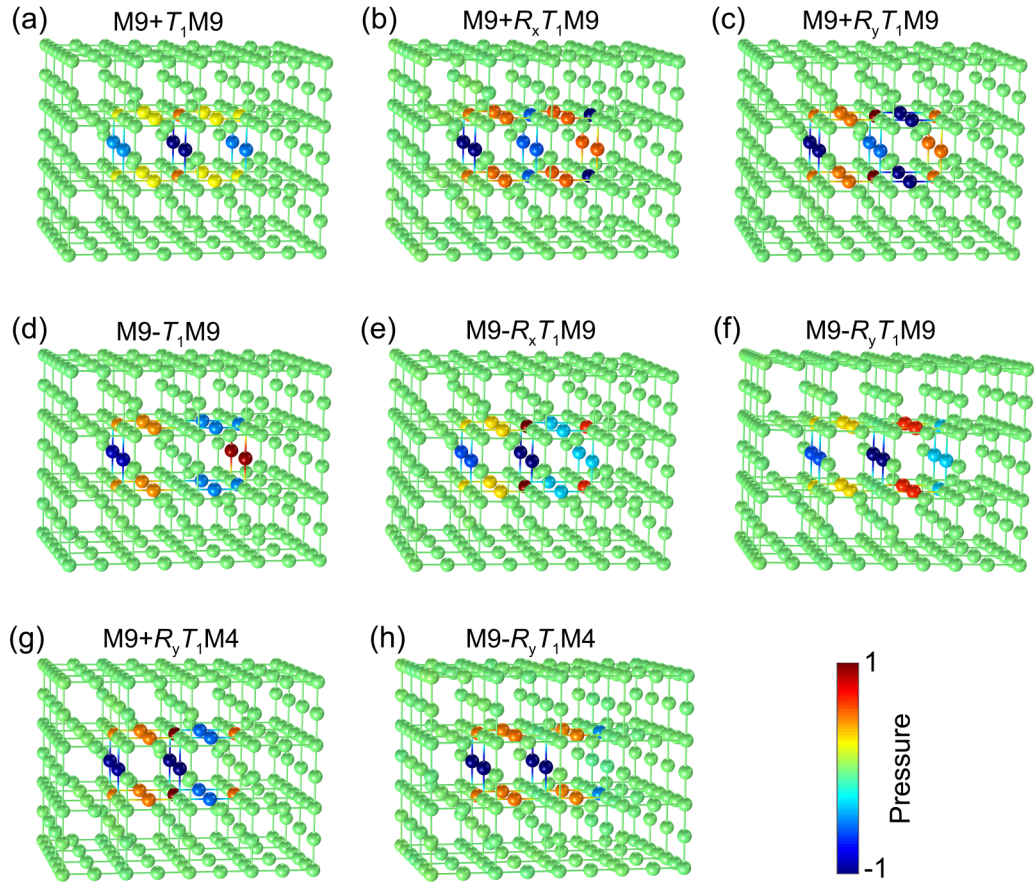


FIG. 8. The simulations on different composite flat-band bound states, where the sound pressures are normalized with respect to their maxima, respectively.

At any given wave number k , by projecting Eq. (B6) into the band-vector space $\{u_1(k), u_2(k), u_3(k), u_4(k)\}$ in Eq. (4), we will obtain the occupation probabilities of dispersive band vectors $u_1(k)$ and $u_4(k)$ as

$$\begin{aligned}
 c_{1,4} &= \langle u_{1,4} | \psi_0 \rangle \\
 &= \frac{1}{\sqrt{2}} \left(\mp 1, \frac{\gamma_x(1 + e^{-ik_x})}{\varepsilon}, \frac{\gamma_y(1 + e^{-ik_y})}{\varepsilon}, \frac{\gamma_z(1 + e^{-ik_z})}{\varepsilon} \right) \begin{bmatrix} 0 \\ p_B(1 + e^{-ik_y})(1 + e^{-ik_z}) \\ p_C(1 + e^{-ik_x})(1 + e^{-ik_z}) \\ p_D(1 + e^{-ik_x})(1 + e^{-ik_y}) \end{bmatrix} \\
 &= \frac{(1 + e^{-ik_x})(1 + e^{-ik_y})(1 + e^{-ik_z})}{\sqrt{2}\varepsilon} (p_B\gamma_x + p_C\gamma_y + p_D\gamma_z). \tag{B7}
 \end{aligned}$$

APPENDIX C: SIMULATION AND EXPERIMENTS ON COMPOSITE FLAT-BAND STATES

In this part, we show the simulation and experiment results on the composite flat-band states. The structural parameters are the same as those in Fig. 5. In Fig. 7, the chosen excitation primitive cells locate at the centers of the designed cubic lattices. The excitation frequency $f = 150$ Hz. To analyze the excitation state in a convenient manner, the excitation primitive cells are expanded into 2D planes as shown at the top of every subfigure, where “0” and “ π ” denote that the excitation modes are out of phase. “+” and “-” indicate that

the acoustic pressures are in-phase and out-of-phase excited. The results in Fig. 7 show that there exist 11 elementary flat-band bound states in total with different sound pressure distributions in a primitive cell. Here the mode 9 is actually the flat-band bound state that is discussed in Figs. 3(d) and 5(b).

Figure 8 shows the simulated sound pressure distributions of eight composite flat-band bound states. It should be mentioned that the composite flat-band bound states can be easily constructed by superposing a number of elementary flat-band bound states in Fig. 7. In Fig. 8, T_1 denotes that the flat-band bound state is translated by one primitive cell. R_α denotes

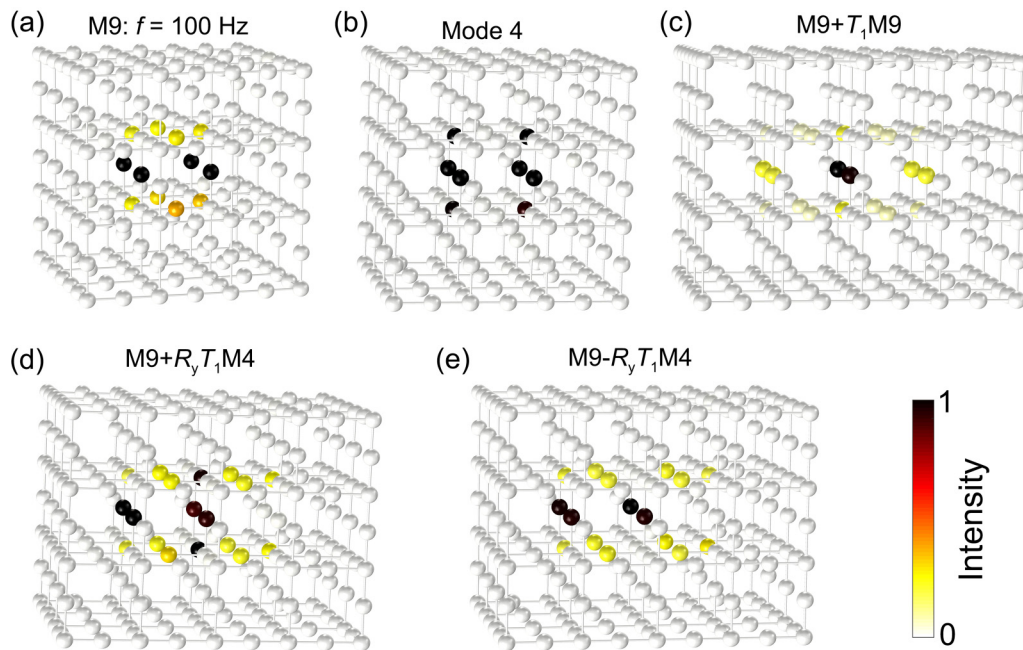


FIG. 9. The experimental results on different composite flat-band bound states, where the sound intensities are normalized with respect to their maxima, respectively. The excitation frequencies are 100 Hz in (a) and 150 Hz in (b)–(e).

that the flat-band bound state is rotated by 90° around the α axis. Figure 9 shows the measured normalized intensity

distributions corresponding to some chosen cases in Figs. 7 and 8.

-
- [1] P. W. Anderson, Absence of diffusion in certain random lattices, *Phys. Rev.* **109**, 1492 (1958).
- [2] M. Segev, Y. Silberberg, and D. N. Christodoulides, Anderson localization of light, *Nat. Photonics* **7**, 197 (2013).
- [3] S. Graham, L. Piche, and M. Grant, Experimental Evidence for Localization of Acoustic Waves in Three Dimensions, *Phys. Rev. Lett.* **64**, 3135 (1990).
- [4] R. L. Weaver, Anderson localization of ultrasound, *Wave Motion* **12**, 129 (1990).
- [5] H. F. Hu, A. Strybulevych, J. H. Page, S. E. Skipetrov, and B. A. van Tiggelen, Localization of ultrasound in a three-dimensional elastic network, *Nat. Phys.* **4**, 945 (2008).
- [6] J. Dhillon, A. Bozhko, E. Walker, A. Neogi, and A. Krokhin, Localization of ultrasound in 2D phononic crystal with randomly oriented asymmetric scatterers, *J. Appl. Phys.* **129**, 134701 (2021).
- [7] F. Izrailev, A. A. Krokhin, and N. M. Makarov, Anomalous localization in low-dimensional systems with correlated disorder, *Phys. Rep.* **512**, 125 (2012).
- [8] D. G. Zhao, Y. X. Shen, Y. Zhang, X. F. Zhu, and L. Yi, Bound states in one-dimensional acoustic parity-time-symmetric lattices for perfect sensing, *Phys. Lett. A* **380**, 2698 (2016).
- [9] F. G. Wu, Z. L. Hou, Z. Y. Liu, and Y. Y. Liu, Point defect states in two-dimensional phononic crystals, *Phys. Lett. A* **292**, 198 (2001).
- [10] J. D. Wang, J. K. Yang, and Z. G. Chen, Two-dimensional defect modes in optically induced photonic lattices, *Phys. Rev. A* **76**, 013828 (2007).
- [11] S. H. Jo, H. J. Yoon, Y. C. Shin, M. Kim, and B. D. Youn, Elastic wave localization and harvesting using double defect modes of a phononic crystal, *J. Appl. Phys.* **127**, 164901 (2020).
- [12] H. Y. Fan, B. Z. Xia, L. Tong, S. J. Zheng, and D. J. Yu, Elastic Higher-Order Topological Insulator with Topologically Protected Corner States, *Phys. Rev. Lett.* **122**, 204301 (2019).
- [13] X. D. Chen, W. M. Deng, F. L. Shi, F. L. Zhao, M. Chen, and J. W. Dong, Direct Observation of Corner States in Second-Order Topological Photonic Crystal Slabs, *Phys. Rev. Lett.* **122**, 233902 (2019).
- [14] X. P. Zhou, J. Wu, and Y. F. Wu, Topological corner states in non-Hermitian photonic crystals, *Opt. Commun.* **466**, 125653 (2020).
- [15] X. J. Zhang, L. Liu, M. H. Lu, and Y. F. Chen, Valley-Selective Topological Corner States in Sonic Crystals, *Phys. Rev. Lett.* **126**, 156401 (2021).
- [16] W. Y. Deng, J. Y. Lu, F. Li, X. Q. Huang, M. Yan, J. H. Ma, and Z. Y. Liu, Nodal rings and drumhead surface states in phononic crystals, *Nat. Commun.* **10**, 1769 (2019).
- [17] S. Y. Yao and Z. Wang, Edge States and Topological Invariants of Non-Hermitian System, *Phys. Rev. Lett.* **121**, 086803 (2018).
- [18] R. Okugawa, R. Takahashi, and K. Yokomizo, Second-order topological non-Hermitian skin effects, *Phys. Rev. B* **102**, 241202(R) (2020).
- [19] D. Zou, T. Chen, W. He, J. Bao, C. H. Lee, H. Sun, and X. Zhang, Observation of hybrid higher-order skin-topological effect in non-Hermitian topological circuits, *Nat. Commun.* **12**, 7201 (2021).

- [20] H. Friedrich and D. Wintgen, Physical realization of bound states in the continuum, *Phys. Rev. A* **31**, 3964 (1985).
- [21] D. C. Marinica, A. G. Borisov, and S. V. Shabanov, Bound States in the Continuum in Photonics, *Phys. Rev. Lett.* **100**, 183902 (2008).
- [22] Y. Plotnik, O. Peleg, F. Dreisow, M. Heinrich, S. Nolte, A. Szameit, and M. Segev, Experimental Observation of Optical Bound States in the Continuum, *Phys. Rev. Lett.* **107**, 183901 (2011).
- [23] C. W. Hsu, B. Zhen, J. Lee, S. L. Chua, S. G. Johnson, J. D. Joannopoulos, and M. Soljačić, Observation of trapped light within the radiation continuum, *Nature (London)* **499**, 188 (2013).
- [24] B. Zhen, C. W. Hsu, L. Lu, A. D. Stone, and M. Soljačić, Topological Nature of Optical Bound States in the Continuum, *Phys. Rev. Lett.* **113**, 257401 (2014).
- [25] C. W. Hsu, B. Zhen, A. D. Stone, J. D. Joannopoulos, and M. Soljačić, Bound states in the continuum, *Nat. Rev. Mater.* **1**, 16048 (2016).
- [26] M. Minkov, I. A. D. Williamson, M. Xiao, and S. Fan, Zero-Index Bound States in the Continuum, *Phys. Rev. Lett.* **121**, 263901 (2018).
- [27] A. Cerjan, C. W. Hsu, and M. C. Rechtsman, Bound States in the Continuum through Environmental Design, *Phys. Rev. Lett.* **123**, 023902 (2019).
- [28] M. Filoche and S. Mayboroda, Strong Localization Induced by One Clamped Point in Thin Plate Vibrations, *Phys. Rev. Lett.* **103**, 254301 (2009).
- [29] G. Lefebvre, A. Gondel, M. Dubois, M. Atlan, F. Feppon, A. Labbé, C. Gillot, A. Garelli, M. Ernoult, S. Mayboroda, M. Filoche, and P. Sebbah, One Single Static Measurement Predicts Wave Localization in Complex Structures, *Phys. Rev. Lett.* **117**, 074301 (2016).
- [30] Y. X. Shen, Y. G. Peng, D. G. Zhao, X. C. Chen, J. Zhu, and X. F. Zhu, One-Way Localized Adiabatic Passage in an Acoustic System, *Phys. Rev. Lett.* **122**, 094501 (2019).
- [31] D. Guzmán-Silva, C. Mejía-Cortés, M. A. Bandres, M. C. Rechtsman, S. Weimann, S. Nolte, M. Segev, A. Szameit, and R. A. Vicencio, Experimental observation of bulk and edge transport in photonic Lieb lattices, *New J. Phys.* **16**, 063061 (2014).
- [32] R. A. Vicencio, C. Cantillano, L. Morales-Inostroza, B. Real, C. Mejía-Cortés, S. Weimann, A. Szameit, and M. I. Molina, Observation of Localized States in Lieb Photonic Lattices, *Phys. Rev. Lett.* **114**, 245503 (2015).
- [33] S. Mukherjee, A. Spracklen, D. Choudhury, N. Goldman, P. Öhberg, E. Andersson, and R. R. Thomson, Observation of a Localized Flat-Band State in a Photonic Lieb Lattice, *Phys. Rev. Lett.* **114**, 245504 (2015).
- [34] J. D. Bodyfelt, D. Leykam, C. Danieli, X. Q. Yu, and S. Flach, Flatbands Under Correlated Perturbations, *Phys. Rev. Lett.* **113**, 236403 (2014).
- [35] F. Baboux, L. Ge, T. Jacqmin, M. Biondi, E. Galopin, A. Lemaître, L. Le-Gratiet, I. Sagnes, S. Schmidt, H. E. Türeci, A. Amo, and J. Bloch, Bosonic Condensation and Disorder-Induced Localization in a Flat Band, *Phys. Rev. Lett.* **116**, 066402 (2016).
- [36] J. Patterson and B. Bailey, *Solid-State Physics: Introduction to the Theory*, 2nd ed. (Springer-Verlag Berlin/Heidelberg, Berlin, 2010).
- [37] J. K. Asbóth, L. Oroszlány, and A. Pályi, *A Short Course on Topological Insulators: Band Structure and Edge States in One and Two Dimensions* (Springer International Publishing, Switzerland, 2016).
- [38] V. I. Kukulkin, V. M. Krasnopol'sky, and J. Horacek, *Theory of Resonances: Principles and Applications* (Springer, The Netherlands, 1989).
- [39] S. Fan and J. D. Joannopoulos, Analysis of guided resonances in photonic crystal slabs, *Phys. Rev. B* **65**, 235112 (2002).
- [40] S. Fan, W. Suh, and J. D. Joannopoulos, Temporal coupled-mode theory for the Fano resonance in optical resonators, *J. Opt. Soc. Am. A* **20**, 569 (2003).